

# The nature of the dense core population in the Pipe Nebula: A survey of $\text{NH}_3$ , CCS, and $\text{HC}_5\text{N}$ molecular line emission

J. M. Rathborne, C. J. Lada, A. A. Muench

*Harvard-Smithsonian Center for Astrophysics, 60 Garden Street, Cambridge, MA 02138,  
USA: jrathborne@cfa.harvard.edu, clada@cfa.harvard.edu, gmuench@cfa.harvard.edu*

and

J. F. Alves

*Calar Alto Observatory, Centro Astronómico Hispano Alemán, c/Jesús Durbán Remón  
2-2, 04004, Almeria, Spain: jalves@caha.es*

and

M. Lombardi

*European Southern Observatory, Karl-Schwarzschild-Str. 2, 85748 Garching, Germany:  
mlombard@eso.org*

## ABSTRACT

Recent extinction studies of the Pipe Nebula ( $d=130$  pc) reveal many cores spanning a range in mass from 0.2 to 20.4  $M_\odot$ . These dense cores were identified via their high extinction and comprise a starless population in a very early stage of development. Here we present a survey of  $\text{NH}_3$  (1,1),  $\text{NH}_3$  (2,2), CCS (2<sub>1</sub>–1<sub>0</sub>), and  $\text{HC}_5\text{N}$  (9,8) emission toward 46 of these cores. An atlas of the 2MASS extinction maps is also presented. In total, we detect 63% of the cores in  $\text{NH}_3$  (1,1), 22% in  $\text{NH}_3$  (2,2), 28% in CCS, and 9% in  $\text{HC}_5\text{N}$  emission. We find the cores are associated with dense gas ( $\sim 10^4 \text{ cm}^{-3}$ ) with  $9.5 \leq T_K \leq 17$  K. Compared to  $\text{C}^{18}\text{O}$ , we find the  $\text{NH}_3$  linewidths are systematically narrower, implying that the  $\text{NH}_3$  is tracing the dense component of the gas and that these cores are relatively quiescent. We find no correlation between core linewidth and size. The derived properties of the Pipe cores are similar to cores within other low-mass star-forming regions: the only differences are that the Pipe cores have weaker  $\text{NH}_3$  emission and most show no current star formation as evidenced by the lack of embedded infrared sources. Such weak  $\text{NH}_3$  emission could arise due to low column densities and abundances or reduced excitation due to relatively

low core volume densities. Either alternative implies that the cores are relatively young. Thus, the Pipe cores represent an excellent sample of dense cores in which to study the initial conditions for star formation and the earliest stages of core formation and evolution.

*Subject headings:* stars: formation–dust, extinction–ISM: globules–ISM: molecules

## 1. Introduction

The Pipe Nebula, at a distance of 130 pc, is one of the closest molecular cloud complexes in the Galaxy. With a mass of  $10^4 M_\odot$ , it spans  $\sim 48$  degs<sup>2</sup> on the sky but contains little evidence for active star formation. In addition to tracing the larger-scale molecular gas associated with the Pipe Nebula, a <sup>12</sup>CO, <sup>13</sup>CO, and C<sup>18</sup>O(1–0) (highly undersampled) survey of the region (Onishi et al. 1999) detected a small number of dense cores. The densest of these, associated with the dark cloud B59, appears to be the only site within the Pipe Nebula where active star formation is occurring. Indeed, recent *Spitzer* observations reveal an embedded cluster of young stellar objects within B59 (Brooke et al. 2007).

Recent extinction studies of the Pipe Nebula (Lombardi et al. 2006; Alves, Lombardi, & Lada 2007) reveal many compact dust cores that likely represent incipient sites of star formation. These cores were identified using 2MASS extinction maps derived from the JHK photometry of over 4.5 million stars (Fig. 1; Lombardi et al. 2006). The individual compact cores were extracted from the larger-scale, more diffuse lower-column density material associated with the molecular cloud via a wavelet transform technique (see Alves et al. 2007). In total, 159 cores were identified and span a range in peak  $A_v$  and core mass and are distributed throughout the Pipe Nebula (Alves et al. 2007). This large sample represents a critical data base for measuring the initial conditions for star formation and testing theories of core formation and evolution. Indeed, the dense core mass function (CMF) generated from these cores reveals a similarity to the shape of the stellar initial mass function (IMF; e.g. Alves et al. 2007) with the profound implication that the stellar IMF is in fact pre-determined by the form of the CMF. The origin of the stellar IMF may be, therefore, directly linked to the origin of dense cores.

While the Pipe Nebula represents an excellent example of a molecular cloud in a very early stage of star formation, little work has been done to ascertain the dynamical and evolutionary status of its cores. Our aim is to study these cores in detail via the combination of their extinction and molecular line properties; the extinction map reveals measurements of the core masses and sizes while the molecular line observations reveal the kinematics and

gas temperatures within the cores. To this end, we are conducting extensive ground- and space-based surveys of the cores located within the Pipe Nebula. The Pipe cores are well suited for studies of core formation and evolution because they are distributed over a large area, are well separated and well defined, and represent a complete sample of dense cores within a single cloud with accurate masses in the mass range of  $\sim 0.2$  to  $20.4 M_{\odot}$ .

To begin, we have obtained  $\text{C}^{18}\text{O}$  (1–0) observations toward a sample of 94 cores distributed throughout the nebula. The details of these observations and results are presented in Muench et al. (2007). In brief summary, all cores show strong  $\text{C}^{18}\text{O}$  emission, have measured linewidths,  $\Delta V$ , of  $\sim 0.14 - 0.61 \text{ km s}^{-1}$ , and show no size-linewidth correlation.

Because  $\text{C}^{18}\text{O}$  (1–0) emission traces all molecular gas along the line of sight, the measured  $\text{C}^{18}\text{O}$  linewidths will trace both the lower density intercore material in addition to the dense gas associated with the core. To isolate the emission from the dense core, we have also obtained  $\text{NH}_3$  observations toward a sample of the Pipe cores and report the results of these observations here. Because  $\text{NH}_3$  requires such high densities to be excited ( $> 10^4 \text{ cm}^{-3}$ ), only the densest gas will exhibit significant  $\text{NH}_3$  emission. Thus,  $\text{NH}_3$  observations will reveal the fraction of cores in the Pipe Nebula that contain dense gas. Determination of the dense core fraction and how it varies across the core mass function and with kinematical state will provide crucial data for understanding the evolutionary status of these objects.

The combination of the extinction and molecular line studies ( $\text{C}^{18}\text{O}$  and  $\text{NH}_3$ ), and the implications for core formation and evolution, is discussed in Lada et al. (2007), the third paper in this series on the Pipe Nebula. By accurately measuring the linewidths from the  $\text{NH}_3$  (1,1) emission in each core, and by combining this with measurements of the core masses, one can determine the fraction of cores that are unbound and the core stability, which can provide important clues to their formation and evolution. Indeed, Lada et al. (2007) find that the majority of Pipe cores are pressure confined, gravitationally unbound objects whose properties are dominated by thermal processes in a pressurized medium.

Ammonia has been used extensively to study both high- and low-mass star-forming regions (e.g. Myers & Benson 1983; Benson & Myers 1989; Jijina et al. 1999). Because it is the least depleted species in, and, thus, the most reliable tracer of, cold dense gas within starless cores, we use  $\text{NH}_3$  to trace the densest gas in the Pipe Nebula. The 18 individual hyperfine components of the  $\text{NH}_3$  (1,1) transitions can be used to measure the intrinsic one dimensional velocity dispersion ( $\sigma_v$ ), optical depth ( $\tau$ ), and excitation temperature ( $T_{\text{ex}}$ ). Observations of the  $\text{NH}_3$  (2,2) transition were also obtained in order to directly measure the gas temperatures of the brightest cores in the sample. Ratios of the  $\text{NH}_3$  (1,1) and (2,2) lines reveal the kinetic temperature ( $T_K$ ) and, therefore, density of the cores.

To probe the very densest gas and to determine the chemical evolution of the cores, we also obtained CCS ( $2_1-1_0$ ) and HC<sub>5</sub>N (9,8) observations. These molecules are found in very dense starless cores (e.g. Benson & Myers 1983; Suzuki et al. 1992). The abundance of carbon-chain molecules (e.g. CCS and HC<sub>5</sub>N) compared to NH<sub>3</sub> is thought to trace the chemical evolution of cores; carbon-chain molecules being more abundant in the very earliest stages in core evolution, compared to NH<sub>3</sub> which is more abundant in the later stages (e.g. Suzuki et al. 1992). Thus, the combination of these data can reveal the youth and star-forming potential of the cores.

In this paper, we present the results of a survey for NH<sub>3</sub> (1,1), NH<sub>3</sub> (2,2), CCS ( $2_1-1_0$ ), and HC<sub>5</sub>N (9,8) emission toward a sample of 46 of the extinction cores identified in the Pipe Nebula. All but one of these cores has been observed as part of the C<sup>18</sup>O survey (Muench et al. 2007). We find that most cores are indeed associated with dense gas. Their measured linewidths are narrow, with several cores having linewidths comparable to their thermal linewidths. The derived properties ( $T_K$ , intrinsic  $\Delta V$ , non-thermal  $\Delta V$ , radius) of the cores within the Pipe Nebula are similar to cores within other low-mass star-forming regions: the only difference is that the Pipe cores typically have weaker NH<sub>3</sub> emission and most show no current star formation.

## 2. Observations and Data Reduction

The observations were obtained using the 100-m Robert C. Byrd Green Bank Telescope (GBT) from 2006 October to 2007 February. The NH<sub>3</sub> (1,1) NH<sub>3</sub> (2,2) CCS ( $2_1-1_0$ ), and HC<sub>5</sub>N (9,8) transitions were observed simultaneously using the K-band (upper) receiver. Table 1 lists the frequencies for each of these transitions.

All spectra were obtained in the frequency switched mode ( $\Delta\nu = 4$  MHz). The spectrometer was set up with a bandwidth of 12.5 MHz, which produced a frequency resolution of 1.846 kHz (velocity resolution of 0.023 km s<sup>-1</sup>). The GBT beam width at these frequencies is  $\sim 30''$ .

Due to time constraints, a sub-sample of the complete list of cores identified by Alves et al. (2007) were observed. In total, 46 of the 159 cores were observed and were selected to span a range in peak  $A_v$ , core mass, and location within the Pipe Nebula. The completeness of our sample based on the original catalog of Alves et al. (2007) is shown in Figure 2 as a function of both peak  $A_v$  and core mass. The peak  $A_v$  for the selected cores ranged from 5.3 to 23.7 magnitudes, while their masses range from 0.4 to 20.4  $M_\odot$ ; all cores in the original sample with peak  $A_v > 14$  magnitudes and with masses  $> 4 M_\odot$  were observed.

Spectra were obtained toward the position of peak extinction for each core (these positions are listed in Table 2). The cores were originally identified from 2MASS extinction maps ( $\Theta_{HPBW} \sim 1'$ ; Alves et al. 2007). Because the coordinates listed in the catalog of Alves et al. (2007) refer to the centroid and not necessarily the position of peak extinction, the pointing centers for each core were selected by eye to correspond to the true extinction peak. Thus, the coordinates listed here may differ slightly from the positions reported in the catalog of Alves et al. (2007).

Toward some of these cores we have also obtained higher-angular resolution extinction maps using the 3.5 m ESO New Technology Telescope (NTT;  $\Theta_{HPBW} \sim 15''$ ; Roman-Zuniga 2007). In many cases, we found sub-structure at higher-angular resolution. Where possible, therefore, we used the higher-angular resolution extinction maps to pinpoint the position of peak extinction. We found that the extinction peaks could differ by as much as  $\sim 1'$  from the quoted positions in the Alves et al. (2007) catalog. Thus, for the cores in which we have obtained these higher-angular resolution extinction maps, we use the coordinates of the peak extinction derived from them. These cores are marked with an asterisk in Table 2.

For the majority of cores, four  $\sim 5$  minute integrations were combined for a total of 18 minutes on source. Toward the brightest 4 cores only a single 5 minute spectrum was obtained. For three cores showing very faint  $\text{NH}_3$  (1,1) emission, we combined additional data for an on source integration time of over 70 minutes. The integration times, system temperatures ( $T_{sys}$ ), source elevation (El), and  $1\sigma$  rms for the spectra are listed in Table 2. Because the system temperatures for the individual frequencies varied by  $< 5\%$ , we quote a single system temperature and, hence,  $1\sigma$  rms for each core.

The pointing and focus were checked at the beginning of each observing session using a nearby, bright pointing source. The pointing corrections were typically  $\sim 8''$  in Azimuth and  $\sim 1''$  in Elevation. The flux density scale was determined from observations of 3C286 (known flux density of 2.38 Jy was taken from Ott et al. 1994).

The spectra were converted from the raw data format into fits files using the SDFITS package. All subsequent data reduction and analysis was performed using the GBTIDL package. The individual polarizations for each spectrum were combined and averaged before opacity and elevation corrections were applied. A first order baseline was removed from all spectra using user-defined baseline windows. All quoted temperatures are  $T_A^*$  (K).

The observations were taken at low elevations ( $\sim 19^\circ$ ) where the pointing model of the GBT is less reliable. As a result, the temperatures of the observations may be in error,

either due to unintended pointing offsets or pointing drifts during the integrations <sup>1</sup>. To quantify the repeatability of the observations, we obtained a spectrum toward the core FeSt 1-457 (our core 109) during each observing session. These data show a variation in peak temperature ( $T_A^*$ ) of  $\sim 10\%$ , while the linewidths show a variation of  $\sim 3\%$  (these values were estimated by fitting two Gaussians to the blended central hyperfine components). Thus, while the temperatures listed may be uncertain, the linewidths and derived parameters (e.g.  $\tau$ ,  $T_K$ ,  $T_{ex}$ ), which are derived from the line ratios and, hence, independent of the absolute scale, will be reliable.

### 3. Results

The  $NH_3$  (1,1),  $NH_3$  (2,2), CCS (2<sub>1</sub>–1<sub>0</sub>), and  $HC_5N$  (9,8) spectra for each core observed in the Pipe Nebula are shown in the Appendix, together with its 2MASS extinction map. We find many cores show little or no detectable  $NH_3$ , CCS, nor  $HC_5N$  emission (e.g. Fig. 36). Many of the remaining cores show only weak  $NH_3$  emission from the central blended hyperfine components (e.g. Fig. 41). A number of cores show weak  $NH_3$  emission, but strong CCS emission (e.g. Fig. 51). Only a small fraction of the cores show strong  $NH_3$  emission. Toward these cores, we clearly see the satellite components in addition to the central blended hyperfine components (e.g. Figs. 30 and 53).

#### 3.1. Determining line parameters: $T_A^*$ , $\sigma_v$ , $V_{LSR}$ .

##### 3.1.1. $NH_3$ (1,1)

We find 12 cores that show bright  $NH_3$  (1,1) emission from both the central and satellite hyperfine components. To determine their line parameters, we used a forward-fitting routine (for a full description see Rosolowsky et al. 2007). This forward-fitting routine models the spectrum given input physical properties and then optimizes these values via non-linear least squares minimization. This method is in contrast to the usual way of determining physical properties directly from the  $NH_3$  (1,1) to (2,2) line ratios. The advantage of this method is that the uncertainties for the physical parameters can be determined in addition to the covariance among the parameters.

In this model, the gas is assumed to have a slab geometry with uniform properties and

---

<sup>1</sup>The pointing rms during one of the six hour shifts was  $12''$  in azimuth and  $2''$  in elevation.

that the velocity dispersions and excitation temperatures of the transitions are the same, i.e. the gas is in Local Thermodynamic Equilibrium (LTE). Assuming the beam filling factor is unity, the spectrum is entirely determined by five parameters:  $T_K$ ,  $T_{\text{ex}}$ ,  $\tau$ ,  $\sigma_v$ , and  $V_{\text{LSR}}$ . Because the extinction cores are always several times larger than the GBT beam, the assumption that the beam filling factor is unity is valid.

The spectra are easily modelled using this approach when the opacity is high. In the case of low optical depth, however, the parameters  $T_{\text{ex}}$  and  $\tau$  become degenerate and it is not possible to solve for them independently. Instead, the fit is optimized for the free parameter  $\gamma \equiv (T_{\text{ex}} - T_{\text{bg}})\tau$  and, thus, in this case, the spectrum is determined by four free parameters:  $T_K$ ,  $\gamma$ ,  $\sigma_v$ , and  $V_{\text{LSR}}$ .

Table 3 lists the measured  $T_A^*$ ,  $V_{\text{LSR}}$ ,  $\sigma_v$ , and integrated intensity for all cores showing  $\text{NH}_3$  (1,1) emission with detections  $> 3\sigma$ . For the 12 bright cores, the  $V_{\text{LSR}}$  and  $\sigma_v$  were determined using the forward-fitting routine discussed above (these cores are marked with an asterisk in Table 3). The quoted  $T_A^*$  in these cases were measured from a single Gaussian fit to the central blended component. The integrated intensity was calculated by summing the emission across the spectrum (from  $V = -23$  to  $30 \text{ km s}^{-1}$ ).

Toward the remaining 34 cores observed, we find 17 cores with weak  $\text{NH}_3$  (1,1) detections. Because the emission is considerably weaker in these cases, only the central blended components were detected ( $> 3\sigma$ ). Thus, to characterize this emission, we fit a single Gaussian profile to the observed emission. The  $T_A^*$ ,  $V_{\text{LSR}}$ , and integrated intensity ( $I = \int T_A^* \Delta V$ ) measured from these fits are included within Table 3.

Because the central component is a blend of 8 individual hyperfine components, the velocity dispersion determined from fitting a single Gaussian profile to the emission will be overestimated. To constrain theories of core formation and evolution, we require accurate estimates of the core velocity dispersions. Thus, it was necessary to determine the amount by which this measurement of the velocity dispersion was overestimated.

To derive the intrinsic velocity dispersion in the cases where we could not fit the spectra with all 18 hyperfine components, we used a conversion factor calculated from synthetic spectra. The synthetic spectra were generated to cover a range in  $\sigma_v$ ,  $T_{\text{ex}}$ , and  $\tau$ . To each of these spectra, we fit a single Gaussian profile to the central blended components and then compared the measured velocity dispersion to that which was used to generate the spectrum.

To determine the correction factor for all measured velocity dispersions we interpolated the relation to produce a curve converting the measured velocity dispersion to that of the intrinsic velocity dispersion (our derived relation is similar to that modelled by Barranco & Goodman 1998). Thus, the correction factor was determined using this method

and then applied to each velocity dispersion measured from a single Gaussian fit to the central blended hyperfine components (17 cores). These corrected velocity dispersions are quoted in Table 3.

In total, toward the 46 cores observed,  $\text{NH}_3$  (1,1) emission was detected ( $> 3\sigma$ ) in 29 cases ( $\sim 63\%$ ).  $\text{NH}_3$  (1,1) emission was detected toward cores spanning the full range of peak  $A_v$  and core mass within our sample. We find no clear correlation between the measured line parameters and either peak  $A_v$  or core mass. Most ( $\sim 86\%$ ) of the cores have  $T_A^* < 1$  K. The  $V_{LSR}$  measured for the cores range from 3 to 6  $\text{km s}^{-1}$  consistent with the measured  $V_{LSR}$  of the molecular gas associated with Pipe Nebula (as traced by  $\text{C}^{18}\text{O}$ ; Onishi et al. 1999; Muench et al. 2007). This confirms that these cores are indeed located within the large-scale molecular cloud associated with the Pipe Nebula and not either background or foreground objects. The measured velocity dispersions range from  $\sim 0.05$  to  $0.3 \text{ km s}^{-1}$ .

### 3.1.2. $\text{NH}_3$ (2,2), CCS, and $\text{HC}_5\text{N}$

For the  $\text{NH}_3$  (2,2), CCS, and  $\text{HC}_5\text{N}$  emission, we fit a single Gaussian profile to all spectra with a  $> 3\sigma$  detection. Although the  $\text{NH}_3$  (2,2) emission comprise 21 individual hyperfine components, in all cases only the central 12 blended components were detected. Tables 3 and 4 list the peak  $T_A^*$ ,  $V_{LSR}$ ,  $\sigma_v$ , and integrated intensity obtained from these fits.

Toward the 46 cores observed,  $\text{NH}_3$  (2,2) emission was detected in 10 cores ( $\sim 22\%$ ), CCS emission in 13 cores ( $\sim 28\%$ ), and  $\text{HC}_5\text{N}$  emission in 4 cores ( $\sim 9\%$ ).

We find  $\text{NH}_3$  (2,2) detections toward cores spanning the range of peak  $A_v$  and core mass, with the most massive core showing the brightest  $\text{NH}_3$  (2,2) emission. In contrast, we only detect CCS emission for cores with peak  $A_v > 8$  magnitudes and  $\text{HC}_5\text{N}$  emission toward cores with peak  $A_v > 12$  magnitudes. This is expected given that the critical densities of the CCS and  $\text{HC}_5\text{N}$  transitions ( $\sim 10^5 \text{ cm}^{-3}$ ) are higher than for  $\text{NH}_3$  ( $\sim 10^4 \text{ cm}^{-3}$ ) and that there may be differences in their relative abundances due to evolutionary effects.

## 3.2. Physical properties: $T_K$ , $\tau$ , $T_{\text{ex}}$ , $n(\text{H}_2)$ , column densities

The forward-fitting model that was used to derive the  $\sigma_v$  and  $V_{LSR}$  for the cores showing bright  $\text{NH}_3$  emission, also measures the physical properties of the gas. Figure 3 shows the measured  $T_K$ ,  $\tau$ , and  $T_{\text{ex}}$  for the brightest cores as a function of the peak  $A_v$  and core mass.

For the 12 cores showing bright  $\text{NH}_3$  emission we find that the mean  $T_K$  is  $\sim 12 \pm 2$  K.



However, for the cores with masses  $> 5 M_{\odot}$  we find  $T_K$  of  $\sim 10 \pm 1$  K, while cores with masses  $< 5 M_{\odot}$  have  $T_K$  of  $\sim 13 \pm 3$  K (the errors quoted here correspond to the standard deviation). Because  $T_K$  is measured from the ratios of the  $\text{NH}_3$  (1,1) to (2,2) lines, this calculation is independent of assumptions about the beam filling factor. The measured opacities for all the cores range from  $\sim 2$  to 10, with a single core having a  $\tau$  of  $\sim 20$  (this is FeSt 1-457, our core 109). The typical  $T_{\text{ex}}$  was  $\sim 5 \pm 1$  K.

In the low optical depth regime, the values of  $\tau$  and  $T_{\text{ex}}$  become degenerate, so the fitting routine optimizes the value of the parameter  $\gamma$  ( $\propto \tau T_{\text{ex}}$ ). For the 5 cores that were found to lie in the optically thin regime, the values of  $\tau T_{\text{ex}}$  are plotted in the lower panel of Figure 3. These cores all have masses  $< 5 M_{\odot}$  and calculated values of  $\tau T_{\text{ex}}$  ranging from 0.5 to 2.

To verify the values of  $T_K$  output from the forward-fitting model, we have also calculated the rotation temperature,  $T_R$ , which is related to  $T_K$  via (Swift et al. 2005)

$$T_R = T_K \left\{ 1 + \frac{T_k}{T_0} \ln [1 + 0.6e^{-15.7/T_k}] \right\}^{-1}$$

where  $T_0$  is the energy gap between the two levels (41.5 K). Using this relation we calculate  $T_R$  for the 7 cores with measured  $\tau$  values to be  $\sim 10.2 \pm 0.9$  K. The rotation temperature can also be determined directly from the ratios of the peak  $T_A^*$  for the  $\text{NH}_3$  (1,1) and (2,2) emission via the expression (Ho & Townes 1983)

$$T_R = \frac{-41.5}{\ln \left[ \frac{-0.282}{\tau} \ln \left\{ 1 - \frac{T_A^*(2,2)}{T_A^*(1,1)} (1 - e^{-\tau}) \right\} \right]}$$

where  $\tau$  is the opacity listed in Table 5 and  $T_A^*(1,1)$  and  $T_A^*(2,2)$  are the measured peak temperatures listed in Table 3. Using this expression, we derive  $T_R$  of  $\sim 9.5 \pm 1.8$  K. Thus, while we find that the mean  $T_R$  measured directly from the line ratios is slightly lower than the  $T_R$  calculated from the forward-fitting routine, they are consistent within the errors especially considering the peak  $T_A^*$  are measured from a single Gaussian fit to the central blended components.

Moreover, we find that the measured  $T_R$  is comparable to  $T_K$  within the errors. Martin et al. (1982) show that while  $T_R$  is, in general, lower than  $T_K$ ,  $T_R$  is a good indicator of the  $T_K$  for kinetic temperatures  $< 20$  K. However,  $T_R$  significantly underestimates  $T_K$  for higher temperatures. Because our measured  $T_K$  values are always lower than 20 K, the similarity of the derived  $T_R$  and  $T_K$  values is expected.

With the determination of  $T_{\text{ex}}$  and  $T_K$ , the  $\text{H}_2$  volume density,  $n(\text{H}_2)$ , can be calculated via the expression (Ho & Townes 1983)

$$n(\text{H}_2) = \frac{A}{C} \left[ \frac{J_\nu(T_{\text{ex}}) - J_\nu(T_{\text{bg}})}{J_\nu(T_k) - J_\nu(T_{\text{ex}})} \right] \left[ 1 + \frac{J_\nu(T_k)}{h\nu/k} \right]$$

where  $A$  is the Einstein  $A$  coefficient ( $1.67 \times 10^{-7} \text{ s}^{-1}$ ; Ho & Townes 1983),  $C$  is the rate coefficient for collision de-excitation ( $8.5 \times 10^{-11} \text{ cm}^3 \text{ s}^{-1}$ ; Danby et al. 1988) and  $J_\nu(T)$  is the Planck function at the given temperature, where,  $J_\nu(T) = h\nu/k (\exp(h\nu/kT) - 1)^{-1}$ . Table 6 lists the  $n(\text{H}_2)$  values for the cores with  $\text{NH}_3$  emission sufficiently bright enough to reliably calculate both  $T_K$  and  $T_{\text{ex}}$ . For these 7 cores we find the  $n(\text{H}_2)$  values ranged from  $0.1$  to  $2.5 \times 10^4 \text{ cm}^{-3}$ . The measured  $n(\text{H}_2)$  derived from the extinction maps for these 7 cores range from  $0.5$  to  $1.3 \times 10^4 \text{ cm}^{-3}$ . In detail, we find that the  $n(\text{H}_2)$  derived from the  $\text{NH}_3$  observations reveal densities typically twice those estimated from the extinction maps. Because the  $n(\text{H}_2)$  derived from the extinction maps represents the mean  $n(\text{H}_2)$  within the core, we expect these values to be lower than the  $n(\text{H}_2)$  calculated from the  $\text{NH}_3$  emission.

With the measured opacity and assuming LTE conditions, we calculate the  $\text{NH}_3$  column density following the method of Olano et al. (1988) via the expression

$$N(\text{NH}_3) = 1.3773 \times 10^{13} Z(T_k) \tau \Delta V T_{\text{ex}}$$

where  $Z(T_k)$  is the partition function (4.417 for  $T_K = 10 \text{ K}$ ; Olano et al. 1988). For this calculation we assume  $T_K = 10 \text{ K}$  and use the measured values of  $\tau$ ,  $T_{\text{ex}}$ , and  $\Delta V$  (where  $\Delta V = 2.35 \sigma_v$ ) for each core. Table 6 lists the values obtained for the cores in which we could determine  $\tau$  and  $T_{\text{ex}}$  (or  $\tau T_{\text{ex}}$ ). For these cores, the  $N(\text{NH}_3)$  was typically  $\sim 4 \times 10^{14} \text{ cm}^{-2}$ .

For CCS,  $\text{HC}_5\text{N}$ , and  $\text{C}^{18}\text{O}$  we assume the emission is optically thin and calculate the column density via

$$N = \frac{3k^2}{8\pi^3 h B} \frac{1}{\mu^2 (J_1 + 1) \nu} \frac{T_{\text{ex}} J_\nu(T_{\text{ex}}) \exp(E_u/kT_{\text{ex}})}{J_\nu(T_{\text{ex}}) - J_\nu(T_{\text{bg}})} \int T_b dV$$

where  $J_1$  is the rotational quantum number of the lower level,  $T_{\text{bg}}$  is the background temperature (2.7 K),  $E_u$  is the energy of the upper level of the transition,  $\mu$  is the dipole moment, and  $B$  is the rotational constant (Table 1 lists the values used for these parameters). The quantity  $\int T_b dV$  is simply the integrated intensity listed from Table 4 (with the appropriate beam efficiency conversion from  $T_A^*$  to  $T_b$ , which is 0.58 for the GBT at these frequencies). For this calculation we assume LTE conditions and that  $T_{\text{ex}} = 10 \text{ K}$ . We find typical  $N(\text{CCS})$

of  $\sim 5 \times 10^{12} \text{ cm}^{-2}$ ,  $N(\text{HC}_5\text{N})$  of  $\sim 3 \times 10^{12} \text{ cm}^{-2}$ , and  $N(\text{C}^{18}\text{O})$  of  $\sim 1 \times 10^{15} \text{ cm}^{-2}$  (see Table 6). The derived column densities will be under estimated if the excitation temperature is lower than the assumed value of 10 K.

For the 17 cores that were detected in  $\text{NH}_3$  (1,1) but showed no  $\text{NH}_3$  (2,2) emission,  $T_K$ ,  $\tau$  or  $T_{\text{ex}}$  could not be determined using the forward-fitting routine, due to its requirement for emission lines in both spectra. In these cases we also calculate the  $\text{NH}_3$  column density assuming that the emission is optically thin using the above expression and that  $T_{\text{ex}}=5 \text{ K}$ . This value of  $T_{\text{ex}}$  was the typical measured  $T_{\text{ex}}$  for the 7 cores for which it could be determined from the  $\text{NH}_3$  hyperfine components. For these 17 cores we find the typical  $N(\text{NH}_3)$  was  $\sim 3 \times 10^{13} \text{ cm}^{-2}$ .

## 4. Discussion

### 4.1. The dense core detection rate

Figure 4 shows the detection rate for the  $\text{NH}_3$  (1,1),  $\text{NH}_3$  (2,2), CCS, and  $\text{HC}_5\text{N}$  transitions as a function of peak  $A_v$  and core mass. Not surprisingly, the detection rate is higher toward those cores with higher peak  $A_v$  and higher mass; in the case of  $\text{NH}_3$  (1,1) we detected emission toward all cores with a peak  $A_v > 15$  magnitudes and with masses  $> 11 M_\odot$ .

Figure 5 shows the histogram of the mean  $\text{H}_2$  volume densities,  $n(\text{H}_2)$ , for the 46 cores surveyed in  $\text{NH}_3$ , obtained from the visual extinction measurements. For this calculation, a spherical volume with radius equal to half the measured size of the core was assumed (as listed in Alves et al. 2007). The masses were calculated from the background subtracted extinction map (see Lada et al. 2007 and Table 2). We find the  $n(\text{H}_2)$  for the complete sample of 46 cores range from 0.4 to  $1.3 \times 10^4 \text{ cm}^{-3}$ . Based on the critical density of  $\text{NH}_3$  ( $n_c \sim 10^4 \text{ cm}^{-3}$ ), we crudely estimate that the detection rate should be  $\sim 17\%$ . Because these volume densities were derived from the extinction maps, they correspond to the mean volume densities within the cores. The fact that we measure a higher detection rate from our observations ( $\sim 63\%$ ) is not surprising given that  $\text{NH}_3$  traces the densest inner parts of a compact core and that the cores most likely have inwardly increasing density gradients.

The detection rate for the  $\text{NH}_3$  (2,2), CCS, and  $\text{HC}_5\text{N}$  transitions are much lower compared to  $\text{NH}_3$  (1,1) likely due to the combination of the fact that higher densities are typically needed for their excitation and that differences in their chemical evolutionary stages will effect their relative abundances. In the case of CCS, its relative distribution to  $\text{NH}_3$  within the cores may differ significantly. In many dense, starless cores the distribution of  $\text{NH}_3$  and CCS emission is noticably different; the  $\text{NH}_3$  emission is typically centrally

concentrated, while the CCS emission arises from a ring-like structure around the  $\text{NH}_3$  core (e.g. Benson & Myers 1983; Velusamy et al. 1995; Kuiper et al. 1996; Hirota et al. 2002). Indeed, morphological differences in the distributions of various depleted molecules, typically carbon bearing species, is clearly seen toward the B68 (our core 101) and FeSt 1-457 (our core 109; Bergin et al. 2002; Aguti et al. 2007).

The non-detection of  $\text{NH}_3$  emission toward many of the cores could arise because of the short integration time per position or because the spectra were not obtained toward the true density peak of the core. Because we are primarily interested in the  $\text{NH}_3$  line ratios and velocity dispersions, our results will not be significantly affected by the fact that we may not be pinpointing the peak of the  $\text{NH}_3$  emission. This will, however, effect the detection rate as we may be missing some emission that falls below our sensitivity limits given the short integration time per point. This is clearly seen in Figure 6 which compares an 18 minute integration to a 74 minute integration toward the same position in two cores (cores 23 and 89). The spectra obtained with the shorter integration time are noiser and, thus, the emission in these cases would not be considered a  $3\sigma$  detection (upper panels). The longer integrations (lower panels) reveal that indeed  $\text{NH}_3$  (1,1) emission does arise from within these cores, albiet the emission is considerably weaker. Given longer integration times per point, the detection rate for these cores would likely increase.

Because only a single spectrum was obtained toward each core, maps are necessary to determine if many of the non-detections may arise due to either inaccurate coordinates from the extinction maps or pointing errors due to the low observing elevations. For 36 of the cores, higher-angular resolution extinction maps, generated from NTT images ( $15''$  angular resolution; Roman-Zuniga 2007), were used to locate the position of peak extinction. For the remaining 13 cores, we used the lower-angular resolution 2MASS extinction maps ( $1'$  angular resolution; Alves et al. 2007). When comparing the positions of peak extinction between the two maps, we found that the position of peak extinction in the higher-angular resolution maps could differ from that obtained from the lower-angular resolution maps by  $\sim 1'$  ( $\sim 2$  GBT beams at these frequencies). In some cases, the extinction cores identified from the 2MASS maps actually consisted of several sub-structures in the higher-angular resolution maps. Thus, the positions obtained for the 13 cores from the 2MASS extinction map may not reflect the true position of peak extinction, or density, in the core at the angular scale of the GBT beam. However, because the cores are resolved in the 2MASS extinction map (typical sizes of  $6'$ ), and with respect to the GBT beam, the positions at which the spectra were obtained will still lie within each of the cores. They may not, therefore, necessarily correspond to the true peak of the extinction, density, nor the peak of the  $\text{NH}_3$  emission. This will be most obvious if the molecular line emission arises from a very compact, dense core. Thus, the non detection in these cases may simply arise due to the fact that we were

not pointing at the best position within the core and that the dense cores may be compact relative to the extinction cores. With only a single spectrum toward the cores it is difficult to rule out potential pointing offsets. Obtaining  $\text{NH}_3$  and CCS maps toward each of the cores will reveal the true density peaks and their relative distributions with respect to the extinction.

Nevertheless, the majority of these cores appear to be bona fide dense cores. We find that the fraction of dense cores within the Pipe Nebula, as traced by  $\text{NH}_3$  (1,1) emission, is 100% for all cores with peak  $A_v > 15$  magnitudes and mass  $> 6 M_\odot$ . This drops to  $\sim 60\%$  for cores with masses  $< 6 M_\odot$ . Deeper observations and mapping could likely raise the detection rate for  $\text{NH}_3$  toward these cores.

#### 4.2. Measured velocity dispersions

Figure 7 shows the measured one dimensional velocity dispersions for cores detected in  $\text{NH}_3$  (2,2), CCS,  $\text{HC}_5\text{N}$ , and  $\text{C}^{18}\text{O}$  as a function of the velocity dispersion measured from the  $\text{NH}_3$  (1,1) emission (the  $\text{C}^{18}\text{O}$  data are from Muench et al. 2007). For gas with  $T_K = 10$  K the thermal velocity dispersions for these molecules are listed in Table 1 and are marked as dotted lines in Figure 7.

These data reveal a strong correlation between the  $\text{NH}_3$  (2,2),  $\text{HC}_5\text{N}$ ,  $\text{C}^{18}\text{O}$ , and  $\text{NH}_3$  (1,1) velocity dispersions. In the case of  $\text{NH}_3$  (2,2), the velocity dispersions are essentially identical to those measured from the  $\text{NH}_3$  (1,1) emission. For the CCS to  $\text{NH}_3$  (1,1) comparison, we see a larger range in the velocity dispersion. We find for  $\text{HC}_5\text{N}$  the velocity dispersions are typically broader than those measured from the  $\text{NH}_3$  (1,1) emission. Because  $\text{HC}_5\text{N}$  is heavier than the  $\text{NH}_3$  molecule (and thus has a smaller thermal velocity dispersion) the fact that the measured velocity dispersion from  $\text{HC}_5\text{N}$  are typically broader than  $\text{NH}_3$ , may indicate that this emission is tracing a larger non-thermal component. With only four detections it is difficult to determine this with certainty.

We find the velocity dispersions measured from the  $\text{NH}_3$  emission are typically narrower than those measured from the  $\text{C}^{18}\text{O}$ : the  $\text{C}^{18}\text{O}$  velocity dispersions are typically 1.4 times broader than  $\text{NH}_3$ . This is expected given the  $\text{C}^{18}\text{O}$  emission will trace all the gas along the line of sight, in contrast to  $\text{NH}_3$ , which traces only the gas associated with the dense compact core. As a result, the  $\text{C}^{18}\text{O}$  observations will over estimate the non-thermal component of the velocity dispersion.

Most cores have velocity dispersions which are about twice their thermal velocity dispersions; the exception being those traced by  $\text{HC}_5\text{N}$  and  $\text{C}^{18}\text{O}$  which show that  $\sigma_v$  is  $\sim 3$  to 4

times broader than thermal. This suggests that the  $\text{NH}_3$ , CCS,  $\text{HC}_5\text{N}$ , and  $\text{C}^{18}\text{O}$  emission is primarily tracing the non-thermal component of the gas. We find that the measured velocity dispersions from the  $\text{C}^{18}\text{O}$  and  $\text{HC}_5\text{N}$  are the comparable for those cores where emission was detected in both transitions. Because carbon species are more depleted in the densest inner core regions, it is likely that both these species arise in the outer most core edges.

We find three cores that have velocity dispersions comparable to the thermal  $\text{NH}_3$  dispersion (assuming gas at 10 K). Although these cores have low signal to noise detections, it may be that they are purely dominated by thermal processes. Using the unique measurement of  $T_K$  for each of the 12 cores where the  $\text{NH}_3$  (1,1) and (2,2) lines were sufficiently strong that the spectra could be modelled (the cores listed in Table 5), we find that the majority of these cores have measured velocity dispersions  $\sim 1$  to 2 times broader than thermal.

With this large sample of cores we can also investigate the size-linewidth relation (e.g. Larson 1981). The data presented here have the advantage of arising from cores within the same cloud which makes comparisons between these properties independent of distance effects. Figure 8 shows the radius versus linewidth plot for cores detected in both  $\text{C}^{18}\text{O}$  and  $\text{NH}_3$  (1,1). While we see the  $\text{C}^{18}\text{O}$  cores (marked with open circles, from Muench et al. 2007) typically have broader linewidths compared to the  $\text{NH}_3$  cores (marked as filled circles), the general trend between these two samples is similar: there appears to be no correlation between the core linewidth and size. As will be discussed in more detail in Lada et al. (2007), the relatively flat distribution of the data within Figure 8 suggests, therefore, that the cores are dominated by thermal rather than turbulent motions. This is also seen toward dense cores in other star forming regions (e.g. Barranco & Goodman 1998; Goodman et al. 1998).

### 4.3. Comparison to other star-forming regions

Past  $\text{NH}_3$  surveys of star forming regions such as Taurus, Ophiuchus, Perseus, Orion, and Cepheus, reveal that the measured properties within these regions showed general trends based on their star formation activity (see Jijina et al. 1999 for a review). For instance, the regions dominated by dense young clusters (e.g. Orion and Cepheus) tend to have higher measured  $T_K$ , linewidths, and core masses. In contrast, Taurus and Ophiuchus have lower values for these properties, however, these cores tend to have higher column densities. Perseus, being intermediate in its star-formation activity, also shows intermediate values for the derived  $\text{NH}_3$  properties (see Jijina et al. 1999 and references therein).

Many of these studies find strong  $\text{NH}_3$  emission and a high detection rate toward the dense cores. However, many of the  $\text{NH}_3$  cores within these surveys are associated with *IRAS*

sources; in the case of Orion, Benson & Myers (1989) found *IRAS* sources coincident with 68% of the  $\text{NH}_3$  cores. Such a high fraction of cores with obvious infrared emission suggests that star formation is already occurring within these cores. Thus, the detection of strong  $\text{NH}_3$  emission in a starless core may imply that the star formation process is imminent. This is consistent with chemical evolutionary models that predict  $\text{NH}_3$  to be most abundant in the later evolutionary stages of core formation (Suzuki et al. 1992).

Our lower  $\text{NH}_3$  detection rate, compared to other  $\text{NH}_3$  surveys of star-forming regions, is consistent with the fact that the Pipe cores have lower densities and most show little signs of active star formation. Indeed, the core associated with B59, the only site within the Pipe Nebula where current star formation is known to be occurring, is one of the few cores that shows very strong  $\text{NH}_3$  emission. Although the detected  $\text{NH}_3$  emission was typically weak toward our sample of cores, these cores do harbor the densest gas within the Pipe Nebula. Moreover, those cores that show strong CCS emission may be the very youngest within the region.

Comparing our measured values for  $T_K$ , the intrinsic  $\Delta V$ , the non-thermal  $\Delta V$ , radius, and column density (Fig. 9) to those measured in other star forming regions reveals that the cores in the Pipe Nebula are most similar to cores within Perseus (see figures within Jijina et al. 1999). The obvious difference between the Perseus cores and those within the Pipe Nebula is the derived column densities and the star formation activity: the Pipe cores show lower column densities and very little star formation.

The lower  $\text{NH}_3$  column densities derived for the Pipe cores could arise because of differences in the intrinsic extinction, abundance of  $\text{NH}_3$ , or excitation conditions compared to other star-forming regions. Because the cores within the Pipe Nebula span a range in peak extinction and core mass similar to other star-forming regions, it seems unlikely that the lower measured column densities arise simply due to differences in their measured extinction. Moreover, the measured column densities of the cores show an order of magnitude greater range ( $10^{13}$ – $10^{15} \text{ cm}^{-2}$ ) compared to the peak extinction (5–20 mags). A more likely scenario is that the intrinsic abundance of  $\text{NH}_3$  is low within many of these cores, possibly due to their relative chemical youth. It may be, however, that the excitation conditions with these cores are insufficient to significantly populate the levels. It is possible that our derived  $\text{NH}_3$  column densities are under estimates and that  $\text{NH}_3$  is more abundant within the cores, but simply not excited to the levels required for strong detections. This is consistent with the relatively low mean densities of the cores ( $\sim 7 \times 10^3 \text{ cm}^{-3}$ ) compared to that necessary to sufficiently populate the observed levels ( $\sim 10^4 \text{ cm}^{-3}$ ). Detailed radiative transfer modelling is required to distinguish between these scenarios.

If we restrict our sample of cores to those with similar column densities as measured

toward other star-forming regions (i.e.  $N(\text{NH}_3) > 10^{14} \text{ cm}^{-3}$ ), we find that the cores within the Pipe share similar properties with cores in both Perseus and Ophiuchus. Given that only 6 cores were detected in the Pipe with such high column densities, it is difficult to determine the distribution in their properties with any certainty. Nevertheless, it appears that the cores in the Pipe Nebula are similar to those found in other low-mass star forming regions. The most noticeable difference is that the majority of Pipe cores tend to show weaker  $\text{NH}_3$  emission and have little star-formation activity.

#### 4.4. Core evolution as traced by column density

The chemical characteristics within dense cold cores can reveal their evolutionary stage. Because they have different production chemistries, the column densities of  $\text{NH}_3$ ,  $\text{CCS}$ ,  $\text{HC}_5\text{N}$ , and  $\text{C}^{18}\text{O}$  can reveal the chemical characteristics in dense cores (e.g. Suzuki et al. 1992). For instance, models for core evolution (Suzuki et al. 1992) predict an anti-correlation between the abundance of  $\text{CCS}$  and  $\text{NH}_3$ ; with  $\text{CCS}$  more abundant in the early evolutionary phases.

Because of the evolutionary effects of depletion and the differences in the molecular distributions within the cores, a single measurement of the column density within the core can only provide limited information on the chemical structure and evolutionary stage. Nevertheless, we find that the comparisons between the column densities of the various species observed within the Pipe cores are similar to what is seen toward dense cores in Taurus and Ophiuchus (Benson & Myers 1989; Suzuki et al. 1992). In particular, we find that: (1) the  $N(\text{NH}_3)$  and  $N(\text{CCS})$  show no clear correlation, which is consistent with differences in the densities of the cores ( $0.5\text{--}2.5 \times 10^4 \text{ cm}^{-3}$ ); (2) the  $N(\text{C}^{18}\text{O})$  is essentially constant for all values of the  $N(\text{CCS})$ , which implies that the  $\text{CCS}$  is a more reliable tracer of denser gas; and (3) that  $N(\text{CCS})$  and  $N(\text{HC}_5\text{N})$  are correlated, which is expected given that these carbon-chain molecules are produced under the same chemical conditions within a core (Fuentes et al. 1990; Suzuki et al. 1992).

We also find high abundance ratios of  $[\text{NH}_3]$  compared to  $[\text{C}^{18}\text{O}]$  for the densest cores, confirming that  $\text{NH}_3$  is a better tracer of dense gas than  $\text{C}^{18}\text{O}$  and that  $\text{C}^{18}\text{O}$  traces the outer core envelope and is depleted in the core centers. Because the chemical abundances trace the evolutionary age of the cores, we can use the fractional abundances of these molecules to estimate the evolutionary ages of the cores. Using the model calculations of Suzuki et al. (1992), we estimate the cores are at an evolutionary age of  $\sim 6 \times 10^5$  years.



## 5. Conclusions

Using the 100 m GBT we have conducted an  $\text{NH}_3$  (1,1),  $\text{NH}_3$  (2,2), CCS (2<sub>1</sub>–1<sub>0</sub>), and  $\text{HC}_5\text{N}$  (9,8) survey toward a sample of 46 cores within the Pipe Nebula. These cores were identified via their high extinction and appear to be dense starless cores which likely represent the initial conditions of star formation. In total, we detect  $\text{NH}_3$  (1,1) emission in 29 cores ( $\sim 63\%$ ),  $\text{NH}_3$  (2,2) emission in 10 cores ( $\sim 22\%$ ), CCS emission in 13 cores ( $\sim 28\%$ ), and  $\text{HC}_5\text{N}$  emission in 4 cores ( $\sim 9\%$ ). Not surprisingly, the detection rate is higher toward those cores with higher peak  $A_v$  and higher mass; in the case of  $\text{NH}_3$  (1,1) we detected emission toward all cores with a peak  $A_v > 15$  magnitudes and with masses  $> 11 M_\odot$ .

We find that the cores are associated with dense ( $> 10^4 \text{ cm}^{-3}$ ) gas. The  $\text{NH}_3$  emission revealed  $n(\text{H}_2)$  typically three times greater than the mean densities measured from the extinction maps. This is expected given that the cores likely have inwardly increasing density gradients; the  $\text{NH}_3$  is tracing the densest centers of the cores.

Using a forward-fitting modelling routine, we estimated the physical properties of the gas ( $T_K$ ,  $\tau$ , and  $T_{\text{ex}}$ ) for 12 cores. We find that  $T_K$  ranges from 9.5 to 17 K, with a median value of  $\sim 12 \pm 2$  K. Cores with higher mass tend to have lower  $T_K$  values ( $10 \pm 1$  K) compared to lower-mass cores ( $13 \pm 3$  K).

The measured one dimensional velocity dispersion,  $\sigma_v$ , for the cores show that the lines are narrow, with several cores having dispersions close to thermal (for a 10 K gas). A comparison between the linewidths measured for the cores from  $\text{C}^{18}\text{O}$  and  $\text{NH}_3$ , reveal that while the general trends are the same, i.e. neither dataset show a size-linewidth relation, the  $\text{NH}_3$  linewidths are systematically lower than those measured from the  $\text{C}^{18}\text{O}$  emission. This arises because the  $\text{C}^{18}\text{O}$  traces all emission along the line of sight, whereas  $\text{NH}_3$  traces only the densest gas associated with the core.

The derived properties of the Pipe cores are similar to dense cores within other star-forming regions, i.e. Perseus, Taurus, Ophiuchus. The most obvious difference is that the cores within the Pipe Nebula typically have weaker  $\text{NH}_3$  emission and most show no evidence for current star formation. The weak  $\text{NH}_3$  emission may arise due to the low abundance of  $\text{NH}_3$  because the cores are chemically young or because the excitation conditions (densities) within the gas are insufficient to excite the observed transitions. Detailed radiative transfer models are needed to resolve this issue.

Although we have a limited number of cores, we estimate their evolutionary ages to be  $\sim 6 \times 10^5$  years. Thus, the cores within the Pipe Nebula represent an excellent sample of dense cores in which to study the initial conditions of star-formation and the earliest stages of core formation and evolution.

We are extremely grateful to Erik Rosolowsky for the use of the  $\text{NH}_3$  forward-fitting routine ahead of publication and for the many informative discussions. We also thank the support staff at the GBT, in particular Frank Ghigo, for help with the observing setup and data reduction. We acknowledge funding support through NASA Origins grant NAG-13041.

## A. Appendix

The 2MASS extinction map and  $\text{NH}_3$  (1,1),  $\text{NH}_3$  (2,2), CCS ( $2_1-1_0$ ), and  $\text{HC}_5\text{N}$  (9,8) spectra for each core are shown in Figs 10 to 55. Labelled in the top left corner of each extinction image is the core number based on the catalog of Alves et al. (2007). In all cases, the extinction images are  $0''.25 \times 0''.25$  and are centered on the peak extinction for the core (as determined from these maps). The grey scale is from an  $A_v$  of 0 to 20 magnitudes. The contour levels are 1.2, 4, 6.8, 9.6, and 12.4 magnitudes ( $3\sigma$  in steps of  $7\sigma$ ). The final image in the appendix, Figure 56, summarises the details of the extinction images and includes the sizes of the 2MASS extinction image angular resolution and the GBT beam.

Each spectrum is centered on the  $V_{LSR}$  of the core (see Tables 3 and 4). The  $\text{NH}_3$  (1,1) spectra extend  $\pm 25 \text{ km s}^{-1}$  while the remaining three spectra extend  $\pm 8 \text{ km s}^{-1}$  around the core's  $V_{LSR}$ . The temperature scale is  $T_A^*$ .

## REFERENCES

- Aguti, E., Lada, C. J., Bergin, E. A., Alves, J. F., & Birkinshaw, M. 2007, ApJ, submitted
- Alves, J., Lombardi, M., & Lada, C. J. 2007, A&A, 462, L17
- Barranco, J. A. & Goodman, A. A. 1998, ApJ, 504, 207
- Benson, P. J. & Myers, P. C. 1983, ApJ, 270, 589
- . 1989, ApJS, 71, 89
- Bergin, E. A., Alves, J., Huard, T., & Lada, C. J. 2002, ApJ, 570, L101
- Brooke, T. Y., et al., ApJ, 655, 364
- Danby, G., Flower, D. R., Valiron, P., Schilke, P., & Walmsley, C. M. 1988, MNRAS, 235, 229
- Fuente, A., Cernicharo, J., Barcia, A., & Gomez-Gonzalez, J. 1990, A&A, 231, 151

- Goodman, A. A., Barranco, J. A., Wilner, D. J., & Heyer, M. H. 1998, *ApJ*, 504, 223
- Hirota, T., Ito, T., & Yamamoto, S. 2002, *ApJ*, 565, 359
- Ho, P. T. P. & Townes, C. H. 1983, *ARA&A*, 21, 239
- Jijina, J., Myers, P. C., & Adams, F. C. 1999, *ApJS*, 125, 161
- Kuiper, T. B. H., Langer, W. D., & Velusamy, T. 1996, *ApJ*, 468, 761
- Lada, C. J., Muench, A. A., Rathborne, J. M., Alves, J. F., & Lombardi, M. 2007, *ApJ*, submitted
- Larson, R. B. 1981, *MNRAS*, 194, 809
- Lombardi, M., Alves, J., & Lada, C. J. 2006, *A&A*, 454, 781
- Martin, R. N., Ruf, K., & Ho, P. T. P. 1982, *Nature*, 296, 632
- Muench, A. A., Lada, C. J., Rathborne, J. M., Alves, J. F., & Lombardi, M. 2007, *ApJ*, submitted
- Myers, P. C. & Benson, P. J. 1983, *ApJ*, 266, 309
- Olano, C. A., Walmsley, C. M., & Wilson, T. L. 1988, *A&A*, 196, 194
- Onishi, T., Kawamura, A., Abe, R., Yamaguchi, N., Saito, H., Moriguchi, Y., Mizuno, A., Ogawa, H., & Fukui, Y. 1999, *PASJ*, 51, 871
- Ott, M., Witzel, A., Quirrenbach, A., Krichbaum, T. P., Standke, K. J., Schalinski, C. J., & Hummel, C. A. 1994, *A&A*, 284, 331
- Roman-Zuniga, C. 2007, *ApJ*, in prep.
- Rosolowsky, E., Pineda, J., Foster, J., Borkin, M., Kauffmann, J., Caselli, P., Myers, P., & Goodman, A. 2007, *ApJS*, in prep.
- Suzuki, H., Yamamoto, S., Ohishi, M., Kaifu, N., Ishikawa, S.-I., Hirahara, Y., & Takano, S. 1992, *ApJ*, 392, 551
- Swift, J. J., Welch, W. J., & Di Francesco, J. 2005, *ApJ*, 620, 823
- Velusamy, T., Kuiper, T. B. H., & Langer, W. D. 1995, *ApJ*, 451, L75+

Table 1: Molecular transition frequencies and constants.

Molecule	Transition	$\nu$ (GHz)	$\mu$ (D)	$E_u$ (cm <sup>-1</sup> )	B (GHz)	Thermal $\sigma_v$ <sup>a</sup> (km s <sup>-1</sup> )
NH <sub>3</sub>	(J,K) = (1,1)	23.694	1.47	16.25	298.117	0.07
NH <sub>3</sub>	(J,K) = (2,2)	22.733	1.47	45.08	298.117	0.07
CCS	$J_N = 2_1-1_0$	22.344	2.81	1.12	6.478	0.04
HC <sub>5</sub> N	J = 9–8	23.963	4.33	4.00	1.331	0.03
C <sup>18</sup> O <sup>b</sup>	J = 1–0	109.782	0.11	3.66	54.890	0.05

<sup>a</sup>Assuming a gas temperature of 10 K.

<sup>b</sup>These data are from Muench et al. (2007). The parameters are included here for completeness when discussing the calculation of column density.

Table 2: Observing parameters

Core <sup>a</sup>	Coordinates		Peak	Mass	$\log[n(\text{H}_2)]^b$	Date	Int.	El	$T_{\text{sys}}$	$1\sigma$ rms
	RA	Dec	$A_v$				time			
	(J2000)	(J2000)	(mag)	( $M_\odot$ )	( $\text{cm}^{-3}$ )		(mins)	( $^\circ$ )	(K)	(K)
6*	17:10:31.57	−27:25:51.59	13.6	3.1	3.9	2006-10-18	22	22	96	0.04
7*	17:11:36.95	−27:33:27.08	12.1	4.7	3.8	2006-11-05	18	17	77	0.04
8*	17:12:12.59	−27:37:20.94	12.2	3.3	3.9	2006-10-18	18	19	102	0.06
11*	17:10:51.00	−27:22:59.54	11.5	3.4	3.8	2006-11-05	18	22	69	0.03
12*	17:11:20.49	−27:26:28.98	18.0	20.4	3.8	2006-10-13	5	16	60	0.06
13	17:10:49.69	−27:13:25.01	5.3	0.5	3.9	2006-10-29	18	19	77	0.04
14*	17:12:34.03	−27:21:16.24	18.5	9.7	3.9	2006-10-13	18	23	52	0.02
15*	17:12:53.38	−27:23:23.98	10.4	2.6	3.8	2006-11-05	18	23	70	0.03
17	17:14:06.81	−27:28:25.97	5.3	0.7	3.9	2006-10-29	69	20	48	0.01
20*	17:15:11.16	−27:35:06.00	9.6	2.3	3.8	2006-11-05	18	21	74	0.04
22*	17:15:48.00	−27:29:32.86	7.7	1.0	3.9	2007-02-08	18	16	50	0.02
23*	17:16:07.19	−27:31:11.97	8.4	1.9	3.8	2006-10-25	74	19	75	0.02
25*	17:16:23.68	−27:10:11.98	6.6	1.1	3.8	2007-02-08	18	18	47	0.02
27*	17:17:07.04	−27:01:48.05	6.6	3.1	3.7	2006-11-05	18	24	68	0.03
30	17:21:01.87	−27:13:42.65	5.3	0.4	3.8	2006-10-29	18	23	68	0.03
31*	17:18:32.07	−26:49:33.57	6.6	1.9	3.7	2006-11-05	18	21	77	0.04
33*	17:19:35.00	−26:55:47.96	10.7	4.3	3.8	2006-11-05	18	21	72	0.04
34*	17:20:18.86	−26:59:18.63	8.4	2.7	3.8	2006-11-05	18	24	68	0.03
36	17:19:29.25	−26:46:18.90	6.6	1.7	3.8	2006-10-29	18	24	66	0.03
37*	17:19:32.21	−26:43:30.06	8.8	2.0	4.1	2006-10-24	18	16	76	0.04
40*	17:21:16.43	−26:52:56.68	23.7	9.2	3.8	2006-10-13	5	24	50	0.05
41*	17:22:29.10	−27:04:03.15	9.8	1.1	4.0	2006-11-26	18	20	75	0.04
42*	17:22:42.12	−27:05:00.58	21.6	2.8	4.1	2006-10-13	18	24	50	0.02
47*	17:27:29.55	−26:59:05.97	10.3	1.4	3.8	2006-10-24	18	21	66	0.03
48*	17:25:59.04	−26:44:11.78	11.1	4.2	3.7	2006-10-18	18	15	120	0.07
51*	17:27:24.00	−26:44:23.99	8.6	1.2	3.8	2006-10-24	18	14	90	0.04
56*	17:28:10.86	−26:24:01.16	11.5	5.2	3.8	2006-10-18	18	18	107	0.06
61*	17:28:38.31	−26:16:55.20	8.9	2.6	3.8	2006-11-26	18	17	84	0.04
62*	17:28:47.94	−26:18:27.05	9.7	2.3	3.7	2006-11-05	18	24	68	0.03
65*	17:31:20.65	−26:30:36.05	11.6	0.7	4.1	2006-10-18	18	20	98	0.05
66*	17:31:15.79	−26:29:06.03	10.9	1.0	4.0	2006-11-05	18	19	84	0.04
70*	17:29:35.59	−25:54:23.39	11.3	1.1	4.0	2006-11-05	18	17	91	0.05
74*	17:32:35.28	−26:15:54.01	12.4	3.0	3.7	2006-11-05	18	19	75	0.04
87*	17:34:11.47	−25:50:15.01	21.0	10.3	3.9	2006-10-14	5	13	67	0.07
89*	17:33:26.56	−25:40:12.01	13.7	1.4	4.0	2006-11-05	74	25	70	0.02
91*	17:32:15.63	−25:25:02.97	11.4	1.1	4.1	2006-11-05	18	15	99	0.05
92*	17:34:06.15	−25:40:03.02	15.1	1.6	4.0	2006-10-18	18	25	87	0.04
93*	17:34:45.21	−25:46:57.09	16.9	3.5	3.9	2007-02-08	18	23	43	0.02
97*	17:33:30.19	−25:31:11.97	14.6	5.9	3.6	2006-11-05	18	14	83	0.04
99*	17:25:06.50	−24:12:48.37	7.3	2.2	4.0	2006-11-05	18	22	76	0.04
101*	17:22:43.12	−23:50:08.51	12.8	1.9	4.1	2006-11-26	18	21	74	0.04
102*	17:34:17.10	−25:34:12.02	19.2	6.7	3.6	2007-02-08	18	25	43	0.02
108	17:31:34.13	−24:58:55.22	7.4	0.8	3.8	2006-10-25	18	19	68	0.03
109*	17:35:48.49	−25:33:05.76	18.3	3.6	3.9	2006-10-13	5	17	58	0.07
113*	17:23:35.71	−23:41:05.63	9.2	2.4	4.0	2006-10-24	18	21	68	0.03
132	17:37:52.80	−25:14:57.51	11.2	4.7	3.7	2006-11-26	18	17	83	0.05

<sup>a</sup>Asterisks denote cores for which the position and value of the peak  $A_v$  was determined from the higher-angular resolution images obtained with the NTT (Roman-Zuniga 2007). The masses for these cores were, however, determined from the 2MASS background subtracted extinction maps.

<sup>b</sup>Calculated from the visual extinction, assuming a spherical volume with radius equal to half the measured size of the core (as listed in Alves et al. 2007).

Table 3: Observed line parameters of  $\text{NH}_3$  (1,1) and  $\text{NH}_3$  (2,2).

Core <sup>a</sup>	$\text{NH}_3$ (1,1)				$\text{NH}_3$ (2,2)			
	$T_A^*$ (K)	$V_{LSR}$ ( $\text{km s}^{-1}$ )	$\sigma_v$ ( $\text{km s}^{-1}$ )	I ( $\text{K km s}^{-1}$ )	$T_A^*$ (K)	$V_{LSR}$ ( $\text{km s}^{-1}$ )	$\sigma_v$ ( $\text{km s}^{-1}$ )	I ( $\text{K km s}^{-1}$ )
6	0.41	3.43	0.09	0.08	–	–	–	–
7	0.12	3.83	0.08	0.02	–	–	–	–
8	0.17	3.47	0.11	0.05	–	–	–	–
11	–	–	–	–	–	–	–	–
12*	4.87	3.20	0.15	1.72	1.37	3.20	0.18	0.58
13	–	–	–	–	–	–	–	–
14*	0.42	3.47	0.14	0.14	0.09	3.52	0.11	0.02
15	0.17	3.60	0.18	0.07	–	–	–	–
17*	0.20	3.38	0.25	0.12	0.06	3.41	0.27	0.04
20*	0.54	3.54	0.17	0.22	0.15	3.55	0.19	0.07
22	0.12	3.72	0.12	0.03	–	–	–	–
23	0.09	3.58	0.07	0.02	–	–	–	–
25	0.13	3.65	0.20	0.06	–	–	–	–
27	–	–	–	–	–	–	–	–
30	–	–	–	–	–	–	–	–
31	–	–	–	–	–	–	–	–
33	–	–	–	–	–	–	–	–
34	–	–	–	–	–	–	–	–
36	–	–	–	–	–	–	–	–
37	–	–	–	–	–	–	–	–
40*	0.98	3.30	0.10	0.23	0.14	3.34	0.12	0.04
41*	0.39	3.69	0.12	0.11	0.11	3.72	0.14	0.04
42*	0.43	3.75	0.11	0.11	0.10	3.87	0.09	0.02
47*	0.22	2.81	0.14	0.07	–	–	–	–
48	–	–	–	–	–	–	–	–
51	–	–	–	–	–	–	–	–
56	–	–	–	–	–	–	–	–
61	–	–	–	–	–	–	–	–
62	–	–	–	–	–	–	–	–
65	0.22	4.98	0.26	0.13	–	–	–	–
66	–	–	–	–	–	–	–	–
70	0.14	3.82	0.23	0.08	–	–	–	–
74	–	–	–	–	–	–	–	–
87*	2.28	4.47	0.14	0.75	0.29	4.46	0.16	0.11
89	0.09	4.45	0.10	0.02	–	–	–	–
91	0.17	4.21	0.07	0.03	–	–	–	–
92	0.17	5.10	0.19	0.08	–	–	–	–
93	0.43	5.17	0.17	0.18	–	–	–	–
97	0.39	3.81	0.21	0.19	–	–	–	–
99	–	–	–	–	–	–	–	–
101*	1.06	3.31	0.09	0.22	0.22	3.33	0.09	0.05
102	0.14	4.87	0.24	0.08	–	–	–	–
108*	0.31	3.22	0.16	0.12	–	–	–	–
109*	3.90	5.75	0.08	0.73	1.22	5.73	0.08	0.22
113	0.16	4.60	0.06	0.02	–	–	–	–
132	0.20	3.91	0.18	0.08	–	–	–	–

<sup>a</sup>Asterisks mark cores for which the  $\text{NH}_3$  (1,1)  $V_{LSR}$  and  $\sigma_v$  were determined via the forward-fitting routine.

Table 4: Observed line parameters of CCS ( $2_1-1_0$ ) and HC<sub>5</sub>N (9,8).

Core	CCS				HC <sub>5</sub> N			
	$T_A^*$ (K)	$V_{LSR}$ (km s <sup>-1</sup> )	$\sigma_v$ (km s <sup>-1</sup> )	I (K km s <sup>-1</sup> )	$T_A^*$ (K)	$V_{LSR}$ (km s <sup>-1</sup> )	$\sigma_v$ (km s <sup>-1</sup> )	I (K km s <sup>-1</sup> )
6	0.23	3.50	0.07	0.03	–	–	–	–
7	–	–	–	–	–	–	–	–
8	–	–	–	–	–	–	–	–
11	–	–	–	–	–	–	–	–
12	0.35	3.47	0.19	0.15	0.58	3.44	0.21	0.29
13	–	–	–	–	–	–	–	–
14	0.14	3.45	0.09	0.03	–	–	–	–
15	–	–	–	–	–	–	–	–
17	–	–	–	–	–	–	–	–
20	–	–	–	–	–	–	–	–
22	–	–	–	–	–	–	–	–
23	–	–	–	–	–	–	–	–
25	–	–	–	–	–	–	–	–
27	–	–	–	–	–	–	–	–
30	–	–	–	–	–	–	–	–
31	–	–	–	–	–	–	–	–
33	–	–	–	–	–	–	–	–
34	–	–	–	–	–	–	–	–
36	–	–	–	–	–	–	–	–
37	0.14	3.32	0.08	0.03	–	–	–	–
40	0.78	3.35	0.06	0.11	0.30	3.34	0.14	0.10
41	–	–	–	–	–	–	–	–
42	0.07	3.86	0.11	0.02	–	–	–	–
47	–	–	–	–	–	–	–	–
48	–	–	–	–	–	–	–	–
51	–	–	–	–	–	–	–	–
56	–	–	–	–	–	–	–	–
61	–	–	–	–	–	–	–	–
62	–	–	–	–	–	–	–	–
65	–	–	–	–	–	–	–	–
66	–	–	–	–	–	–	–	–
70	–	–	–	–	–	–	–	–
74	–	–	–	–	–	–	–	–
87	0.23	4.50	0.25	0.14	–	–	–	–
89	0.06	4.87	0.26	0.04	–	–	–	–
91	–	–	–	–	–	–	–	–
92	0.15	5.04	0.12	0.04	–	–	–	–
93	0.16	5.26	0.17	0.06	–	–	–	–
97	–	–	–	–	–	–	–	–
99	–	–	–	–	–	–	–	–
101	0.55	3.37	0.07	0.09	0.44	3.36	0.15	0.15
102	0.35	4.84	0.08	0.07	–	–	–	–
108	–	–	–	–	–	–	–	–
109	0.44	5.80	0.07	0.07	0.27	5.76	0.12	0.08
113	–	–	–	–	–	–	–	–
132	–	–	–	–	–	–	–	–

Table 5: Derived parameters from the  $\text{NH}_3$  lines.

Core	$T_K$ (K)	$\tau$	$T_{\text{ex}}$ (K)	$T_{\text{ex}}\tau$ (K)
12	$11.3 \pm 0.1$	$10.2 \pm 0.2$	$7.4 \pm 0.0$	–
14	$12.0 \pm 0.4$	$1.0 \pm 0.3$	$4.4 \pm 0.4$	–
17	$17.5 \pm 1.3$	–	–	$0.5 \pm 0.0$
20	$15.2 \pm 0.5$	–	–	$1.7 \pm 0.1$
40	$10.3 \pm 0.5$	$2.4 \pm 0.4$	$5.3 \pm 0.3$	–
41	$14.3 \pm 0.7$	–	–	$1.6 \pm 0.1$
42	$12.4 \pm 0.4$	–	–	$1.9 \pm 0.0$
47	$12.6 \pm 1.0$	$2.5 \pm 0.8$	$3.2 \pm 0.1$	–
87	$9.8 \pm 0.3$	$6.3 \pm 0.3$	$5.4 \pm 0.1$	–
101	$10.4 \pm 0.2$	$5.1 \pm 0.2$	$4.5 \pm 0.1$	–
108	$14.1 \pm 0.8$	–	–	$1.0 \pm 0.0$
109	$9.5 \pm 0.1$	$19.8 \pm 0.3$	$6.6 \pm 0.0$	–



Table 6: Volume and column densities of the brightest cores in the Pipe Nebula.

Core	$\log[n(\text{H}_2)]^a$ ( $\text{cm}^{-3}$ )	$\log[N(\text{NH}_3)]$ ( $\text{cm}^{-2}$ )	$\log[N(\text{CCS})]$ ( $\text{cm}^{-2}$ )	$\log[N(\text{HC}_5\text{N})]$ ( $\text{cm}^{-2}$ )	$\log[N(\text{C}^{18}\text{O})]$ ( $\text{cm}^{-2}$ )
6	–	13.7	12.4	–	15.1
7	–	13.2	–	–	15.1
8	–	13.3	–	–	15.1
12	4.4	15.2	13.1	12.9	–
14	3.7	14.0	12.4	–	15.3
15	–	13.4	–	–	15.2
17	–	13.3	–	–	14.5
20	–	13.6	–	–	14.9
22	–	13.2	–	–	14.7
23	–	13.0	–	–	14.8
25	–	13.3	–	–	14.5
37	–	–	12.3	–	15.0
40	4.0	14.3	13.0	12.4	15.1
41	–	13.4	–	–	15.0
42	–	13.5	12.2	–	15.2
47	3.0	14.2	–	–	15.1
65	–	13.6	–	–	15.2
70	–	13.3	–	–	15.2
87	4.0	14.8	13.0	–	15.1
89	–	13.1	12.5	–	15.1
91	–	13.2	–	–	14.9
92	–	13.4	12.5	–	15.2
93	–	13.8	12.7	–	15.2
97	–	13.8	–	–	14.8
101	3.7	14.5	12.9	12.6	14.9
102	–	13.4	12.7	–	14.9
108	–	13.4	–	–	14.6
109	4.4	15.2	12.7	12.3	15.2
113	–	13.2	–	–	14.9
132	–	13.4	–	–	15.1

<sup>a</sup>Calculated from the  $\text{NH}_3$  data as described in § 3.2.

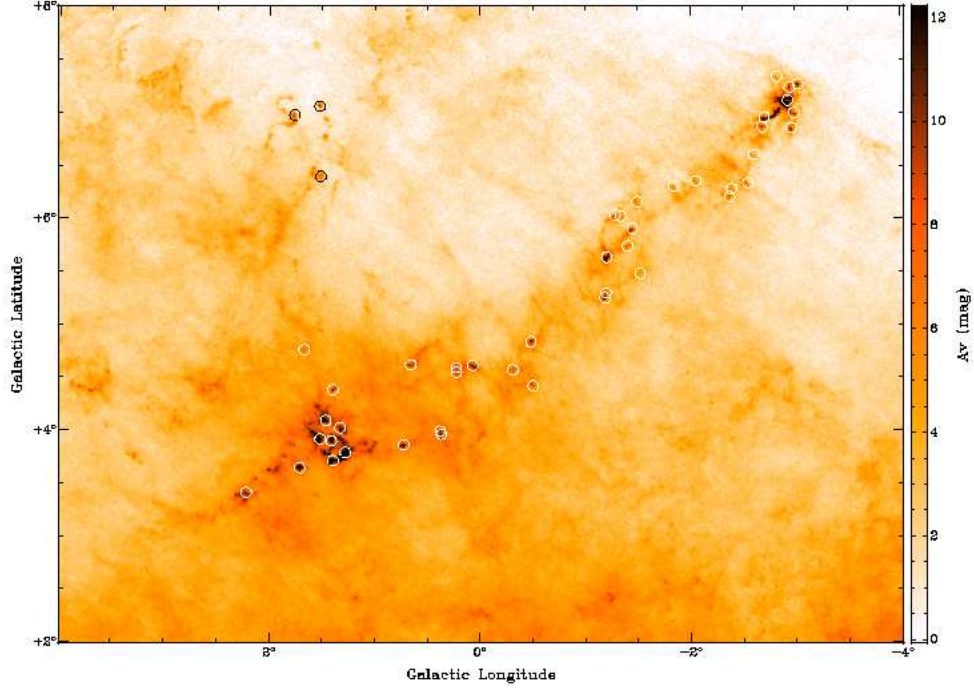


Fig. 1.— The 2MASS extinction map of the Pipe Nebula (Lombardi et al. 2006). This map was derived from the JHK photometry of over 4.5 million stars. Many compact cores are clearly seen in this map in addition to the larger-scale, more diffuse lower-column density material associated with the molecular cloud. Alves et al. (2007) identified 159 compact cores within this region. The 46 cores that comprise our source list are marked with circles. These cores were selected to span a range in peak  $A_v$ , core mass, and location within the Pipe Nebula. We find that the majority of these are associated with dense gas.

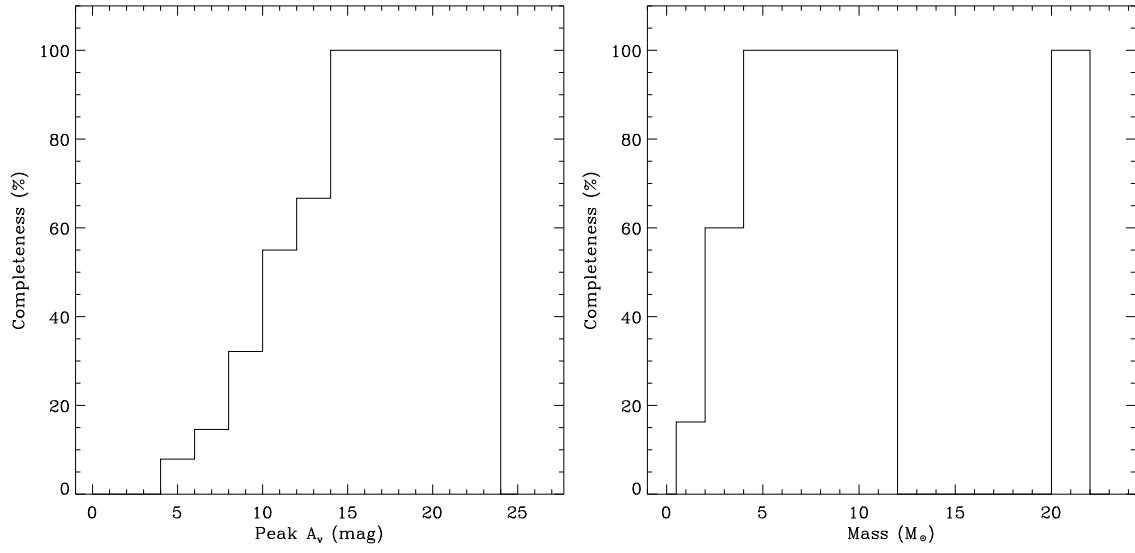


Fig. 2.— The completeness of the observed sample of cores given the original catalog of Alves et al. (2007) as a function of peak  $A_v$  (left) and core mass (right). All cores from the original catalog of Alves et al. (2007) with peak  $A_v > 14$  magnitudes and with masses  $> 4 M_{\odot}$  were observed.

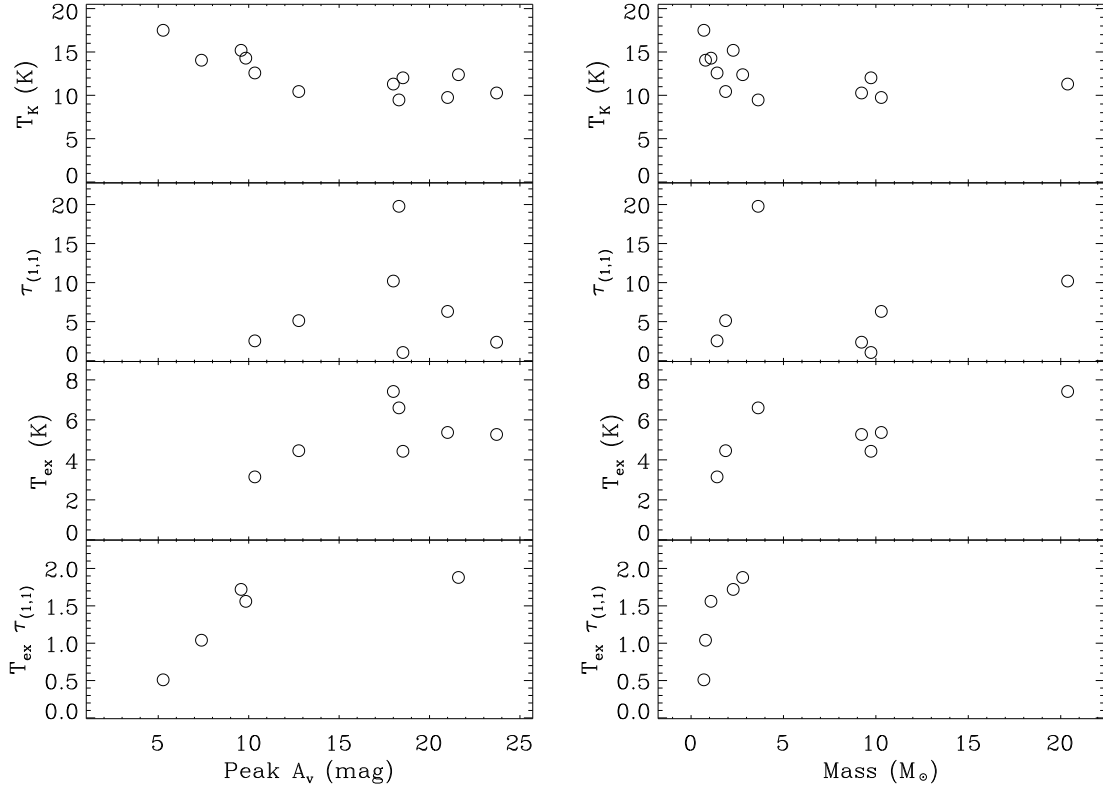


Fig. 3.— The derived parameters,  $T_K$ ,  $\tau$ , and  $T_{\text{ex}}$ , output from the forward-fitting modelling of the cores showing strong  $\text{NH}_3$  emission as a function of peak  $A_v$  (left) and core mass (right). For cores with low opacities, values of  $\tau$  and  $T_{\text{ex}}$  can not be determined independently. The lower panels shows the values of the parameter  $\tau T_{\text{ex}}$  which is used to characterize the emission in the case of low optical depths.

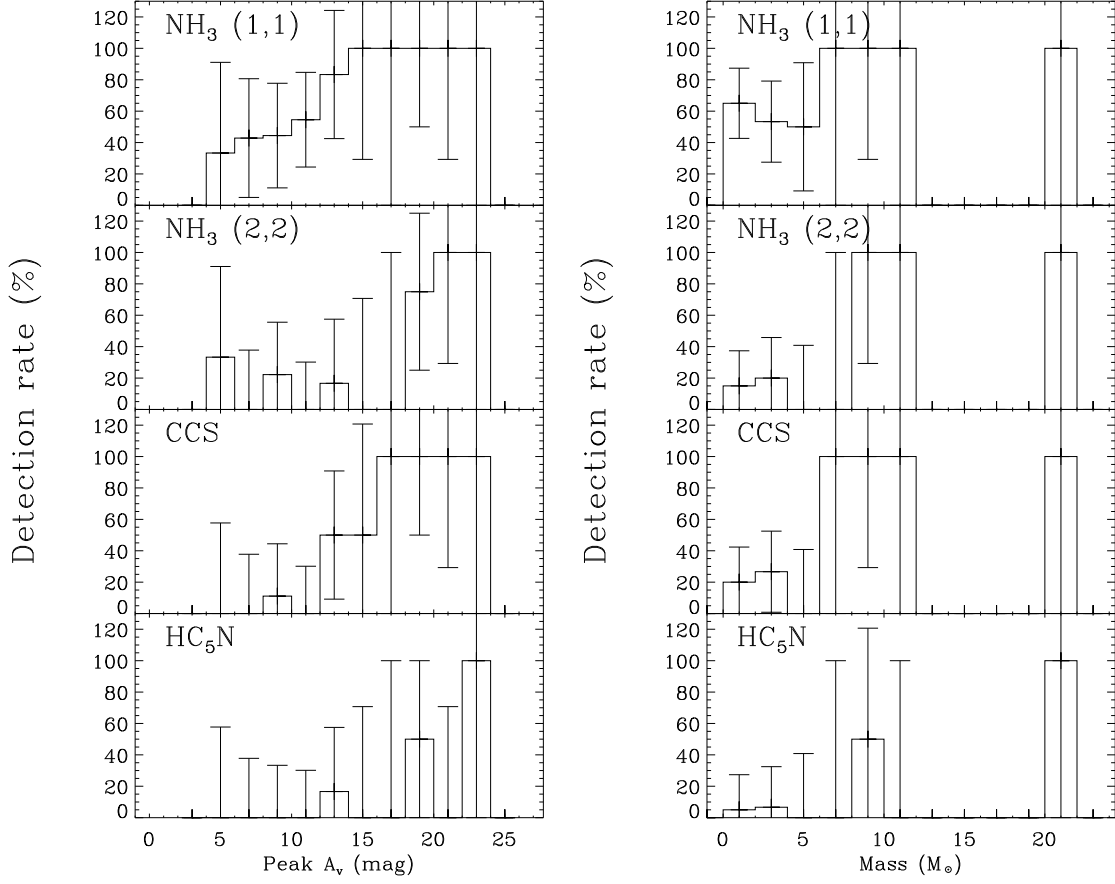


Fig. 4.— The detection rate for each molecular transition as a function of peak  $A_v$  (left) and core mass (right). We detect all  $\text{NH}_3 (1,1)$  emission toward cores with a peak  $A_v > 15$  magnitudes and with masses  $> 11 M_\odot$ .

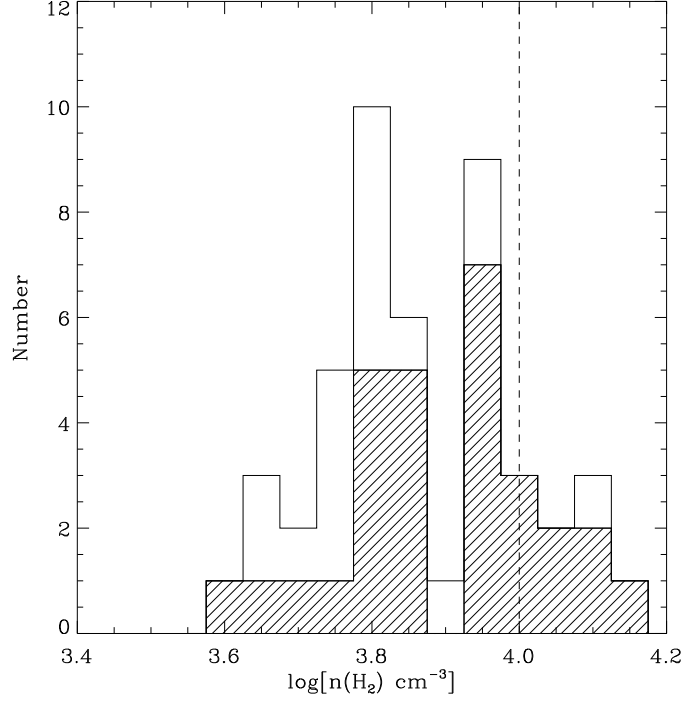


Fig. 5.— The mean volume H<sub>2</sub> density,  $n(\text{H}_2)$ , calculated from the visual extinction measurements for the 46 cores within our sample (open histogram). The diagonal lines mark the  $n(\text{H}_2)$  measured from the extinction maps for the cores detected in NH<sub>3</sub> (1,1). The dotted line marks the critical density of the NH<sub>3</sub> (1,1) transition. We find  $\sim 17\%$  of the cores have mean volume densities greater than the critical density for NH<sub>3</sub>. Our higher measured NH<sub>3</sub> (1,1) detection rate (63%) is expected considering that NH<sub>3</sub> (1,1) traces the densest inner regions within the cores. This is in contrast to the  $n(\text{H}_2)$  measured from the extinction maps which corresponds to the mean volume density within the larger extinction core.

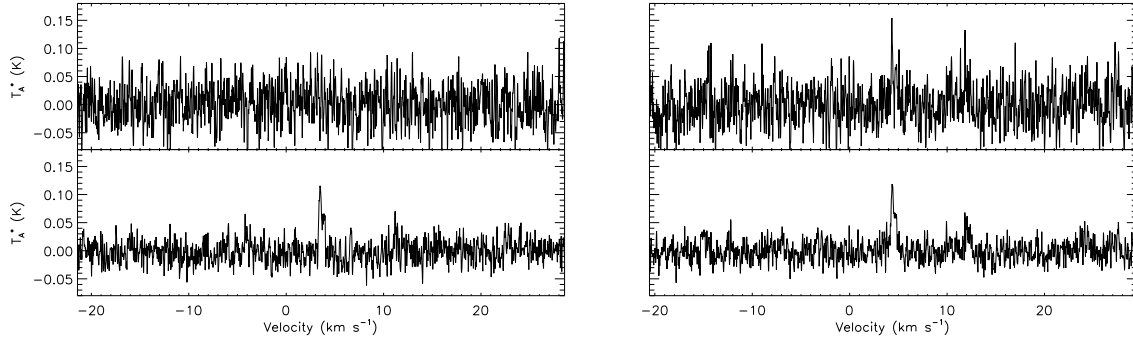


Fig. 6.— The comparison between  $\text{NH}_3$  (1,1) spectra obtained with differing integration times (top:  $t \sim 18$  minutes, bottom:  $t \sim 74$  minutes) for two cores (23 and 89, left and right respectively). The spectra toward the majority of cores were obtained with an integration time of  $\sim 18$  minutes (c.f. top panels). In these two cases, therefore, we would not have detected  $\text{NH}_3$  (1,1) emission. Thus, the non-detection of  $\text{NH}_3$  (1,1) emission may simply be due to the short integration times. With longer integration times per point the detection rate for these cores would likely increase.

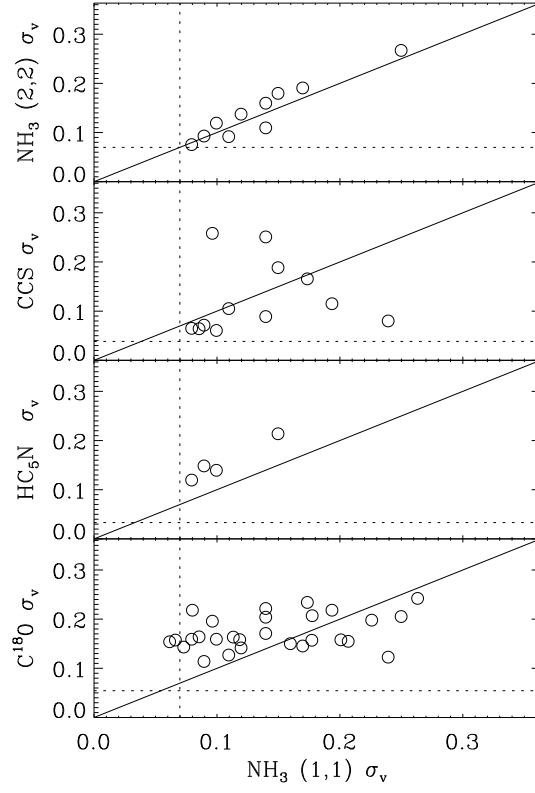


Fig. 7.— Measured one dimensional velocity dispersion for cores with  $\text{NH}_3$  (2,2), CCS,  $\text{HC}_5\text{N}$ , and  $\text{C}^{18}\text{O}$  emission compared to those measured from the  $\text{NH}_3$  (1,1) emission. All axes are in units of  $\text{km s}^{-1}$ . The solid line traces equal values of the dispersions. The dotted lines trace the thermal velocity dispersion for each molecule (assuming 10 K gas).



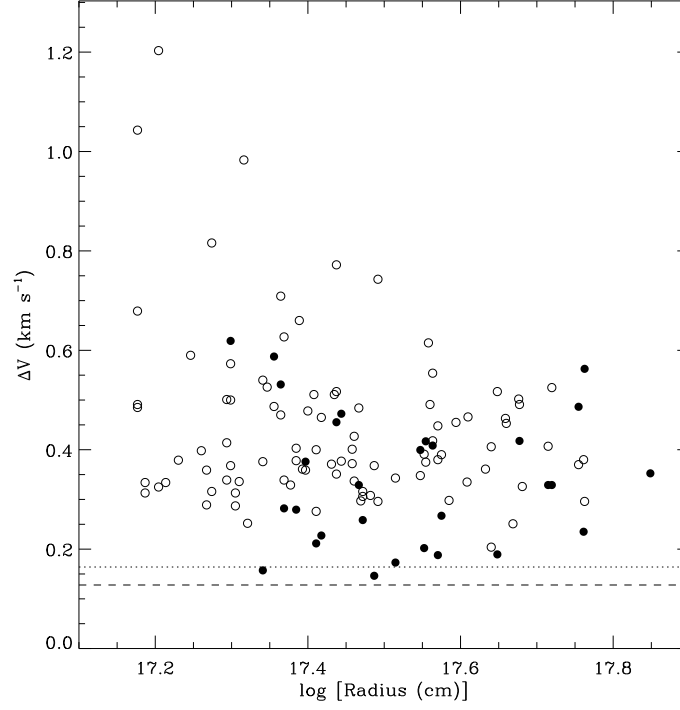


Fig. 8.— Core radius versus linewidth for all cores detected in C<sup>18</sup>O (open circles) and NH<sub>3</sub> (closed circles) emission. While the linewidths measured from the C<sup>18</sup>O are typically broader than those measured from NH<sub>3</sub> emission, there is no correlation between the radius and linewidth in either species for the cores within the Pipe Nebula. The dotted and dashed lines marks the thermal linewidths for NH<sub>3</sub> and C<sup>18</sup>O respectively.

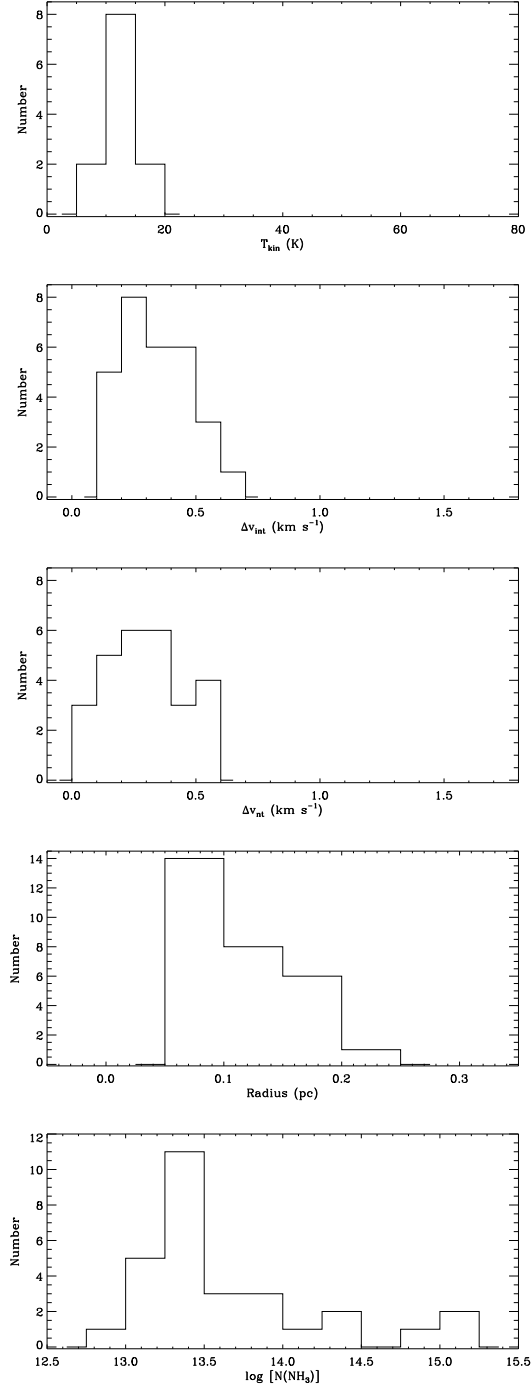


Fig. 9.— Histograms of the derived properties for the cores within the Pipe Nebula. Comparisons between these histograms and similar ones for other star forming regions (e.g. Taurus, Ophiuchus, Perseus, Orion, and Cepheus) reveal the Pipe cores are most similar to cores within Perseus and Ophiuchus. The obvious exception is that the Pipe cores have lower column densities and that the region contains very little active star formation.

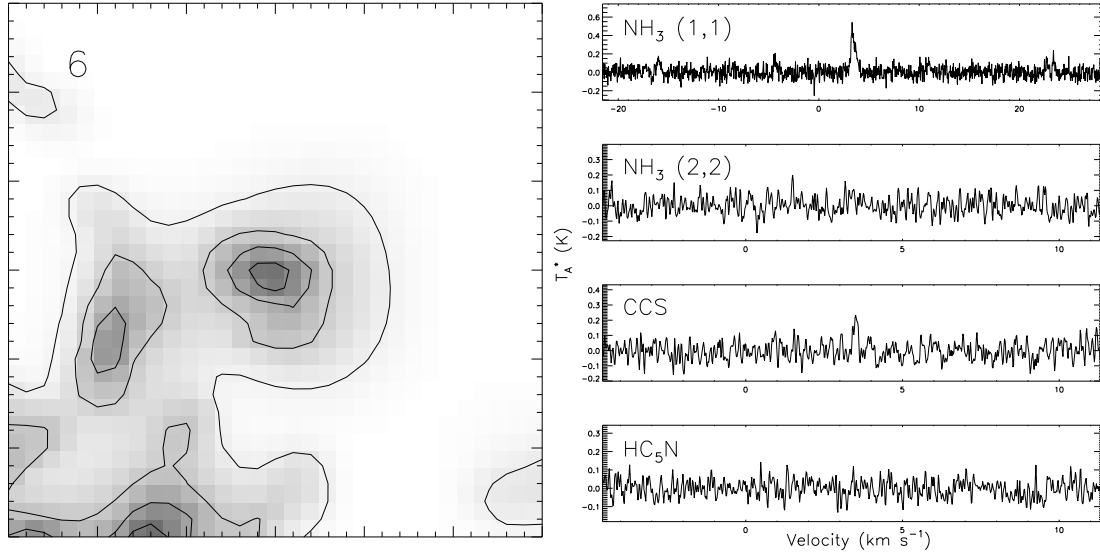


Fig. 10.— The extinction image (left) and spectra (right) toward core 6. See the appendix text for a description of the image and spectra.